nature photonics

ARTICLES

https://doi.org/10.1038/s41566-019-0367-9

Transverse localization of transmission eigenchannels

Hasan Yılmaz[1], Chia Wei Hsu[1], Alexey Yamilov[2] and Hui Cao[1*]

Transmission eigenchannels are building blocks of coherent wave transport in diffusive media, and selective excitation of individual eigenchannels can lead to diverse transport behaviour. An essential yet poorly understood property is the transverse spatial profile of each eigenchannel, which is relevant for the associated energy density and critical for coupling light into and out of it. Here, we discover that the transmission eigenchannels of a disordered slab possess exponentially localized incident and outgoing profiles, even in the diffusive regime far from Anderson localization. Such transverse localization arises from a combination of reciprocity, local coupling of spatial modes and non-local correlations of scattered waves. Experimentally, we observe signatures of such localization even with finite illumination area. The transverse localization of high-transmission channels enhances optical energy densities inside turbid media, which will be important for light–matter interactions and imaging applications.

Spatial inhomogeneities in the refractive index of a disordered medium cause multiple-scattering of light. In disordered media such as biological tissue, white paint and clouds, most of the incident light reflects back, hindering the transfer of energy and information through the media. However, by utilizing the interference of scattered waves, it is possible to prepare optimized wavefronts that completely suppress reflection—a striking phenomenon first predicted in the context of mesoscopic electron transport[1–4]. The required incident wavefronts are the eigenvectors of $t^\dagger t$ where t is the field transmission matrix; the corresponding eigenvalues give the total transmission. In a lossless diffusive medium, the transmission eigenvalues τ span from 0 to 1, leading to closed ($\tau \approx 0$) and open ($\tau \approx 1$) channels. In recent years, spatial light modulators (SLMs) have been used to excite the open channels[5–14] to enhance light transmission through diffusive media. Selective excitation of individual channels can dramatically change the total energy stored inside the random media as well as the spatial distribution of energy density[14–20].

Some important questions regarding the transmission eigenchannels remain open. What are the transverse spatial profiles for coupling light into such channels? Once coupled in, how do the eigenchannels spread in the transverse direction? In the Anderson localization regime of transport, a high-transmission channel is formed by coupled spatially localized modes[21–26], so transversely localized excitation and propagation are expected. However, Anderson localization is extremely hard to achieve in three-dimensional (3D) disordered systems[27], and diffusive transport is much more common. In the diffusive regime, the open channels are expected to cover the entire transverse extent of the system[15,24], utilizing all available spatial degrees of freedom.

Here, we discover that the transmission eigenchannels are transversely localized even in the diffusive regime of transport. In a disordered slab of width W much larger than thickness L, all transmission eigenchannels have a finite transverse extent that is much smaller than W. In the $W \to \infty$ limit, the channel width approaches an asymptotic value D_∞, which scales as $(kl_t)L$ in two dimensions. Here l_t is the transport mean free path and k the effective wavenumber in the slab. Moreover, all eigenchannels feature an exponential decay in their transverse intensity profiles, and they do not spread laterally while propagating through the slab. These properties can be explained in terms of optical reciprocity, the bandedness of the real-space transmission matrix and non-local correlations of multiply scattered waves. The transverse eigenchannel localization in the diffusive regime is a distinct physical phenomenon from the previously known transverse localization in Anderson-localized systems[28–33]. Experimentally, we observe that high-transmission channels are exponentially localized in the transverse directions on both front and back surfaces of a diffusive slab made of ZnO nanoparticles. For finite-area illumination, the transverse extent of a high-transmission channel is smaller than the illumination area, and its lateral spreading in the diffusive slab is suppressed. The transverse localization of high-transmission channels greatly enhances the energy densities of both transmitted light and light inside the slab. It therefore has a potential impact on the advancements of deep-tissue imaging, optogenetics[34–36] and the manipulation of light–matter interactions inside turbid media[37,38].

Transverse localization of eigenchannels

To achieve complete characterization of the transmission eigenchannels we performed numerical simulations where we can exert full control over the incident wavefront and systematically explore the entire parameter space of interest. We first calculated the field transmission matrix t of a 2D diffusive slab using the recursive Green's function method[39], then computed the spatial profiles of individual eigenchannels (see Methods). Remarkably, in wide slabs, we observe that the eigenchannels are exponentially localized in the transverse direction parallel to the slab (an exemplary open channel is shown in Fig. 1a). Even though we impose no constraint on where or how wide the incident wavefront should be, the resulting eigenchannel only occupies a relatively small transverse extent, utilizing just a fraction of the spatial degrees of freedom that are available across the width of the structure. Moreover, the eigenchannel does not spread laterally as it propagates through the disordered slab; the transmitted profile is also localized, with a width similar to that of

[1]Department of Applied Physics, Yale University, New Haven, CT, USA. [2]Department of Physics, Missouri University of Science & Technology, Rolla, MO, USA. *e-mail: hui.cao@yale.edu

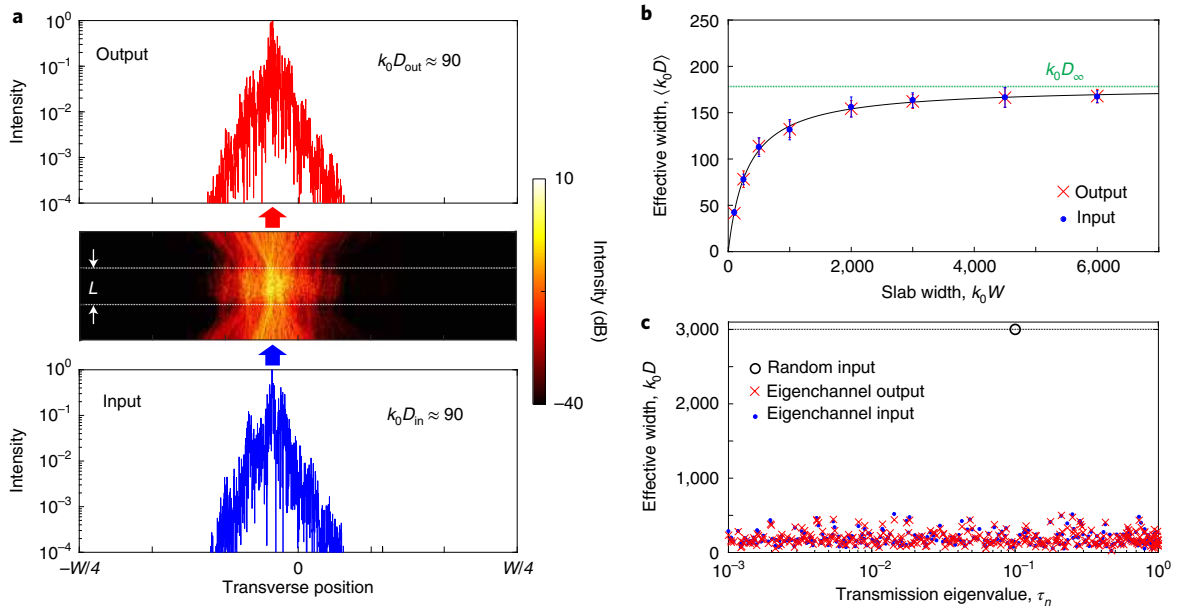

Fig. 1 | Transverse localization of transmission eigenchannels. Numerical results of 2D diffusive slabs with normalized thickness $k_0L = 50$, transport mean free path $n_0k_0l_t = 4.6$, effective refractive index $n_0 = 1.5$ and average transmission eigenvalue $\langle\tau\rangle = 0.10$. $k_0 = 2\pi/\lambda$, where λ is the vacuum wavelength. **a**, Intensity profile of the highest-transmission eigenchannel ($\tau_1 = 0.9999$) in a slab of normalized width $k_0W = 6{,}000$, revealing localization in the transverse direction. White dashed lines in the middle panel indicate the surfaces of the slab, and the relative vertical to horizontal scale is set to 5:1. The log-linear plots of the incident and transmitted intensity profiles on the input and output surfaces of the slab (lower and upper panels) reveal exponential decay in the transverse direction. **b**, Average input and output widths $\langle D_{in}\rangle$ and $\langle D_{out}\rangle$ of open channels ($\tau_n \geq 1/e$) versus slab width k_0W. They are equal and approach an asymptotic value D_∞ (green dashed line) in the wide-slab limit due to transverse localization. Each data point is an average over 10 realizations of structural disorder, and the error bars give the standard deviation among realizations. The black solid line is the fitting that gives D_∞ in the $W \to \infty$ limit. **c**, Eigenchannel widths versus transmission eigenvalues τ_n for $k_0W = 6{,}000$, revealing that all eigenchannels are transversely localized with no lateral spreading from input to output.

the incidence. As shown in the log-linear plot in Fig. 1a, the transverse profile decays exponentially on both input and output surfaces, which is surprising given that the wave transport is diffusive.

A legitimate question is whether such transverse localization of eigenchannels persists in large systems, as experimentally the slab width W is typically so large that it can be regarded as infinite. To find the answer, we carry out a scaling analysis with increasing W. We quantify the width of an eigenchannel via the definition of the participation number (see Methods). As shown in Fig. 1b, input and output channel widths D_{in} and D_{out} are identical after ensemble averaging. In the $W \to \infty$ limit of interest, the open channel remains transversely localized, and its width saturates to an asymptotic value that we denote D_∞. The extrapolation of D_∞ in the $W \to \infty$ limit is described in Supplementary Section 2.4.

The absence of eigenchannel spreading, $\langle D_{in}\rangle = \langle D_{out}\rangle$, can be explained by reciprocity. Lorentz reciprocity requires the scattering matrix to be symmetric[40], so the transmission matrix coming from one side must be the transpose of the transmission matrix coming from the other side. Singular value decomposition of the transmission matrix gives $t = U\sqrt{\tau}V^\dagger$, where the nth columns of V and U are the normalized input and output wavefronts of the nth eigenchannel with transmission eigenvalue τ_n. Since $t^T = V^*\sqrt{\tau}(U^*)^\dagger$, reciprocity demands that the phase conjugation of the nth eigenchannel output must be precisely the input of the nth eigenchannel incident from the other side, with the same eigenvalue. If the disordered medium is statistically equivalent for light incident from either side, the eigenchannel input width must be statistically identical for both directions. Thus the input and output channel widths should be the same after ensemble averaging.

The above argument applies to all eigenchannels, open or closed. Our numerical simulations confirm that all transmission eigenchannels are transversely localized with no lateral spreading, as shown in Fig. 1c. In this example, the widths of all eigenchannels are one order of magnitude smaller than the slab width. The channel width D fluctuates around the mean $\langle D\rangle$ (a histogram of $D/\langle D\rangle$ is presented in Supplementary Fig. 7).

By defining the centre position of an eigenchannel via the centre of mass of its lateral intensity profile, we find that the eigenchannels are randomly and uniformly distributed over the entire width of the slab (Supplementary Fig. 5). An exponential fitting of the tails of their intensity profiles confirms that all eigenchannels decay exponentially in the transverse direction. The decay length is proportional to the channel width, as shown in Supplementary Fig. 7.

Origin of transverse localization

While reciprocity explains the absence of lateral spreading, it remains to be answered why the eigenchannels are transversely localized in the first place. We can gain insight by examining the real-space transmission matrix. Although scattering ensures that light with a specific incident angle is coupled into all outgoing angles once the slab thickness L exceeds the transport mean free path l_t, this is not the case in real space. Given a point-like excitation at the input surface, light spreads laterally as it diffuses through the disordered slab, covering a finite extent of width on the order of L at the output surface (this is shown in Fig. 2a). Such geometric local spreading is the origin of the much celebrated 'memory effect'[41–44]. As a result, the input and output spatial modes are not fully mixed, which emerge as non-vanishing elements only within a distance of $\sim L$ to the diagonal of the real-space transmission matrix (that is, the surface-to-surface Green's function), as shown in Fig. 2b. It is noteworthy that 2D Anderson localization is absent in our systems, because the real-space transmission matrix bandwidth is

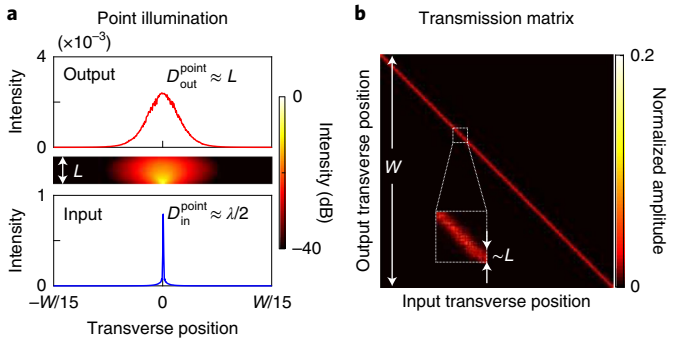

Fig. 2 | Bandedness of the real-space transmission matrix. a, Calculated intensity profile inside a disordered slab when the incident light is focused to a diffraction-limited spot at the front surface, showing the extent of transverse spreading as light diffuses through the slab. D_{in}^{point} and D_{out}^{point} are the beam widths at the input and output surfaces. The intensity profiles shown are ensemble averaged over 1,000 realizations of disorder. **b**, Amplitudes of complex elements of the real-space transmission matrix. While the matrix size is given by the slab width W, only elements within a distance ~L from the diagonal are non-vanishing, because the extent of diffusive spreading in the slab is much less than the slab width. The simulation parameters are the same as in Fig. 1a. Inset: expanded view of a part of the matrix.

proportional to the sample thickness in all of the systems we study here (Supplementary Fig. 4). Similarly, the real-space matrix $t^{\dagger}t$ also exhibits a bandwidth proportional to L.

Random matrices with dominant near-diagonal elements were previously studied in the context of quantum chaos, and it was found that the eigenvectors of such 'banded random matrices' are exponentially localized[45–47]. It is therefore tempting to explain the transverse localization of eigenchannels through the 'bandedness' of real-space transmission matrix for a wide slab. The standard theory of banded random matrices predicts that when the elements of a Hermitian random matrix are non-vanishing within a band of size b, the eigenvectors are localized with participation numbers proportional to b^2 (refs. [45–47]). In the present context, one would then expect the normalized eigenchannel width kD to be on the order of $(kL)^2$ because the dimensionless bandwidth is $b \approx kL$. For the example in Fig. 1, this argument suggests $kD_{\infty} \approx 5{,}600$, as confirmed numerically in Supplementary Fig. 8, but the actual eigenchannel width is only 90. The far smaller channel width indicates a much stronger transverse localization, which is beyond the standard banded random matrix theory.

To explore what determines the asymptotic open channel width D_{∞}, we carried out a systematic study to map out its dependence on the slab thickness L and the transport mean free path l_t. As shown in Fig. 3a, the open channel width D_{∞} scales linearly with the slab thickness L that determines the real-space transmission matrix bandwidth b, in contrast to predictions from the standard banded random matrix theory. Meanwhile, even though l_t does not affect the real-space transmission matrix bandwidth b, we find in Fig. 3b that the open channel width D_{∞} also scales linearly with l_t. A dimensional analysis and the scale invariance of the electromagnetic wave equation indicates a prefactor proportional to the wavenumber $k = n_0 k_0$. Putting these together, we expect a scaling of $D_{\infty} \propto (kl_t)L$. In Fig. 3c we plot the compiled data of D_{∞} as a function of $(kl_t)L$ from $6 \times 6 = 36$ combinations of (L,l_t) for $n_0 = 1.5$ and $6 \times 2 = 12$ combinations of (L,l_t) for $n_0 = 1$; each D_{∞} is extrapolated from 8 widths of W and 10 realizations of disorder (totalling >3,000 configurations). Indeed, we observe the $D_{\infty} \propto (kl_t)L$ scaling. A least-squares fit determines the proportionality constant to be 0.68, close to 2/3. Note that previous studies[15,24] did not find such transverse localization in the diffusive transport regime because the system width W in the previous simulations was not wide enough. Also, note that such eigenchannel width D_{∞} is generally far smaller than the 2D localization length $\xi_{2D} \approx l_t e^{\pi k l_t/2}$.

The reduction in eigenchannel width from kL^2 to kl_tL requires explanations beyond the bandedness of the real-space transmission matrix. The key factor is the correlations among the non-zero matrix elements induced by multiple scattering of light inside the slab, which are referred to as non-local correlations[48–60]. Stronger scattering (smaller kl_t) enhances non-local correlations and leads to tighter transverse localization. When we replace the non-vanishing elements of the real-space transmission matrix with uncorrelated complex Gaussian random numbers, we observe much wider eigenchannel widths that scale as kL^2, as predicted by standard banded random matrix theory (Supplementary Fig. 8).

Extending such scaling study to disordered slabs in 3D is a daunting computational task. Nevertheless, we expect transverse localization of transmission eigenchannels in 3D diffusive systems, because such systems also possess banded real-space transmission matrices, non-local correlations and reciprocity.

Experiments with finite-area illumination

In practical applications, finite-area illumination is commonly used. Accordingly, in this and the next sections we investigate the effects of transverse localization when the size of an illumination beam is smaller than the asymptotic channel width D_{∞}. Experimentally, we measure the spatial profiles of individual eigenchannels at the input and output surfaces of a 3D scattering slab. The sample consists of ZnO nanoparticles that are spin-coated on a cover slide. The thickness of the ZnO layer is about 10 μm, much less than the lateral dimension of the layer (2 cm × 2 cm). The average transmittance of light at a wavelength of 532 nm is approximately 0.2.

We start by measuring the transmission matrix of the disordered slab. A simplified schematic of the experimental set-up is shown in Fig. 4a, with a detailed one given in Supplementary Fig. 1. A spatially uniform monochromatic laser beam at wavelength $\lambda = 532$ nm is modulated by a phase-only SLM. The SLM surface is imaged by a pair of lenses onto the pupil of a microscope objective. The spatial profile of illumination is thus the 2D Fourier transform of the SLM phase pattern. The illumination area is finite, and its width scales inversely with the SLM macropixel size. We use the SLM and a camera (CCD2) to measure the field transmission matrix in k-space, with a common-path interferometry method akin to refs. [13,61]. The number of SLM macro-pixels that modulate the input beam is 2,048, and the number of output speckle grains recorded by the camera is about 15,000.

After measuring the field transmission matrix t, we determine the incident wavefronts of individual eigenchannels from the eigenvectors of $t^{\dagger}t$. Then we display the corresponding phase patterns on the SLM, and record the 2D spatial intensity profiles $I(x,y)$ that are incident on the front surface and transmitted to the back surface of the sample with two cameras (CCD1, CCD3). We define the effective area of such a profile by the 2D participation number A (see Methods) and the effective width $D = 2\sqrt{A/\pi}$.

A random wavefront exhibits an effective width of $D_{in}^{rand} \approx 13$ μm and $D_{out}^{rand} \approx 21$ μm on two sides of the slab (shown in Fig. 4b,c). In contrast, the highest-transmission eigenchannel has narrower spatial profiles at both input and output (Fig. 4d,e): $D_{in}^{high} \approx 10$ μm and $D_{out}^{high} \approx 14$ μm. Its lateral spreading is also less: $\Delta D^{high} = D_{out}^{high} - D_{in}^{high} \approx 4$ μm, in contrast to $\Delta D^{rand} \approx 8$ μm ~ L for random wavefronts. The enhanced lateral confinement and suppressed spreading lead to a significant increase in the energy density inside the slab. On the back surface, the energy density, averaged over the cross-section of the transmitted beam, is enhanced $\left(T^{high}(D_{in}^{rand})^2\right)/\left(\langle T\rangle (D_{in}^{high})^2\right) = 4.4$ times, which is more than twice the enhancement of total transmitted power $T^{high}/\langle T\rangle = 1.95$.

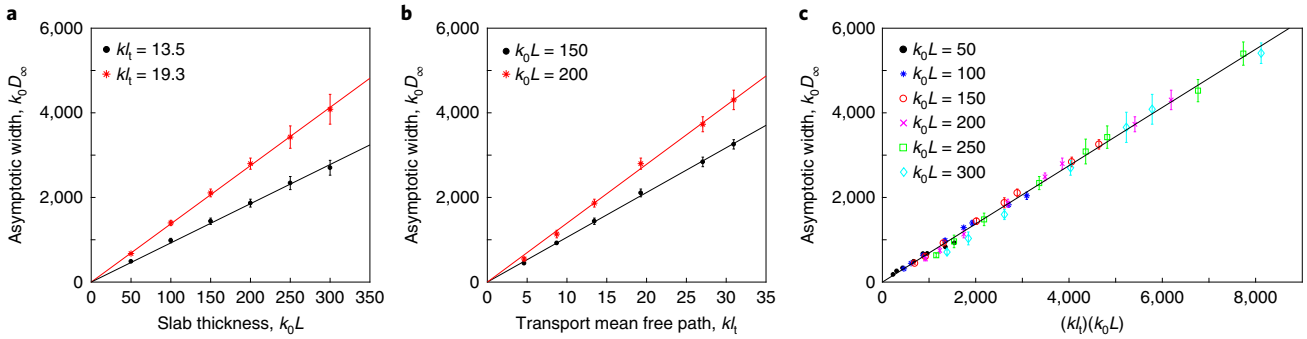

Fig. 3 | Scaling of the asymptotic channel width in diffusive slabs. a, Asymptotic width D_∞ of open channels as a function of slab thickness L when the transport mean free path l_t is fixed. The solid lines represent a linear fit. The slope is smaller when l_t is shorter. **b**, D_∞ as a function of l_t for fixed L. The solid lines are a linear fit, and the slope increases with L. **c**, D_∞ for diffusive slabs of different L, l_t and n_0, showing a general scaling $D_\infty \propto (n_0k_0l_t)L$. Linear regression gives a proportionality constant of 0.68 (black solid line). Each data point represents an ensemble average over all open channels (with $\tau_n \geq 1/e$) in 10 realizations of disorder. Error bars are the standard deviation among the realizations.

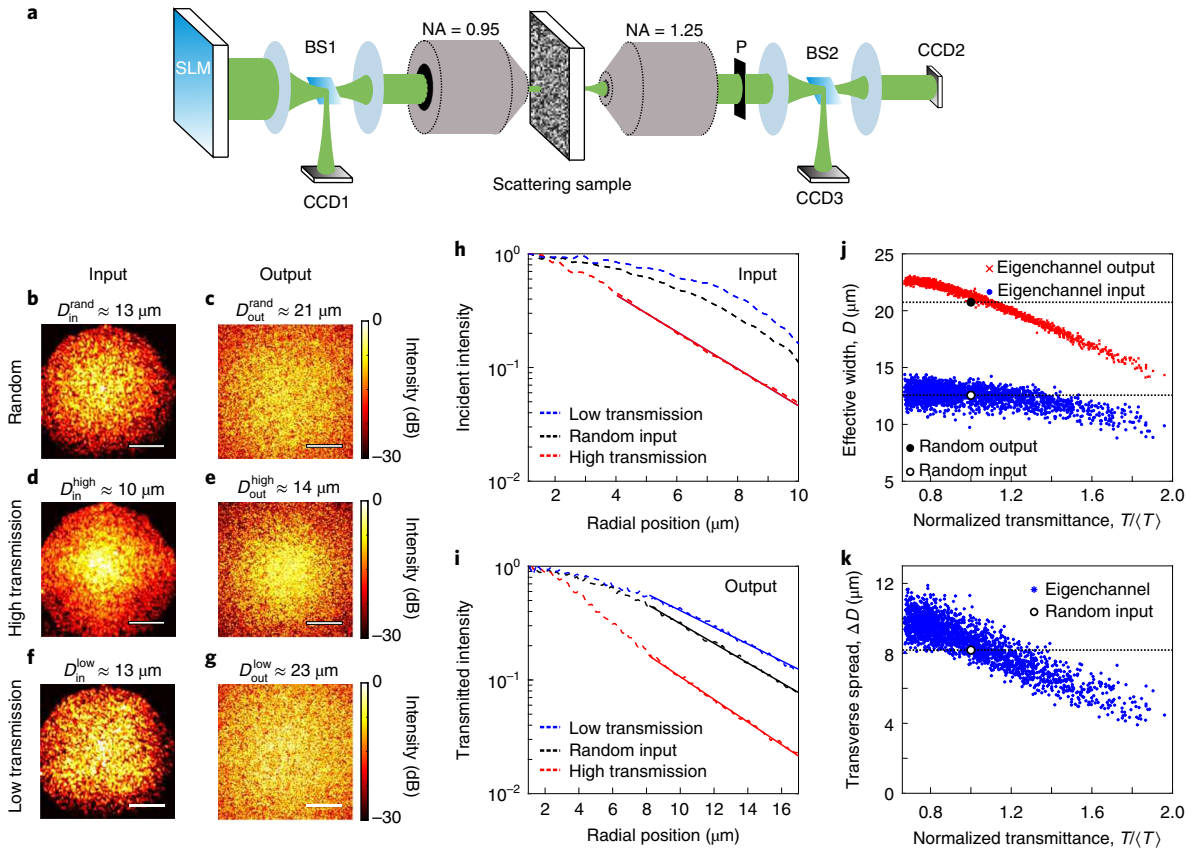

Fig. 4 | Experimental signatures of transverse localization for high-transmission channels. a, Simplified schematic of the experimental set-up for measuring the field transmission matrix of a 3D disordered slab with a finite illumination area, followed by selective excitation of individual transmission eigenchannels and measurement of their incident and transmitted intensity profiles on the front and back surfaces of the sample. BS, beamsplitter; CCD, charge-coupled device camera; NA, numerical aperture; P, linear polarizer. **b**–**g**, Intensity profiles of a random incident wavefront (**b**,**c**), a high-transmission channel (**d**,**e**) and a low-transmission channel (**f**,**g**) on the front (**b**,**d**,**f**) and back (**c**,**e**,**g**) surfaces of the sample. Scale bars, 6 μm. **h**,**i**, Normalized radial intensity profiles of random incident wavefront (black), high-transmission (red) and low-transmission (blue) channels on the front (**h**) and the back (**i**) surfaces of the sample. Dashed lines are measured intensities averaged azimuthally and over 20 random wavefronts or 20 high/low transmission channels. Solid lines are exponential fits to the tails, with decay lengths of 2.6 μm (high-transmission input), 4 μm (high-transmission output), 5 μm (random output) and 6 μm (low-transmission output), respectively. Only high-transmission channels exhibit exponential decay at input. **j**, Input width (blue filled circles) and output width (red crosses) of all 2,048 eigenchannels as a function of the normalized transmittance $T/\langle T\rangle$. Dashed lines denote the input width (black open circle) and output width (black filled circle) for random incident wavefronts. **k**, Transverse spreading $\Delta D = D_{out} - D_{in}$ versus the normalized transmittance $T/\langle T\rangle$ for experimentally measured transmission eigenchannels.

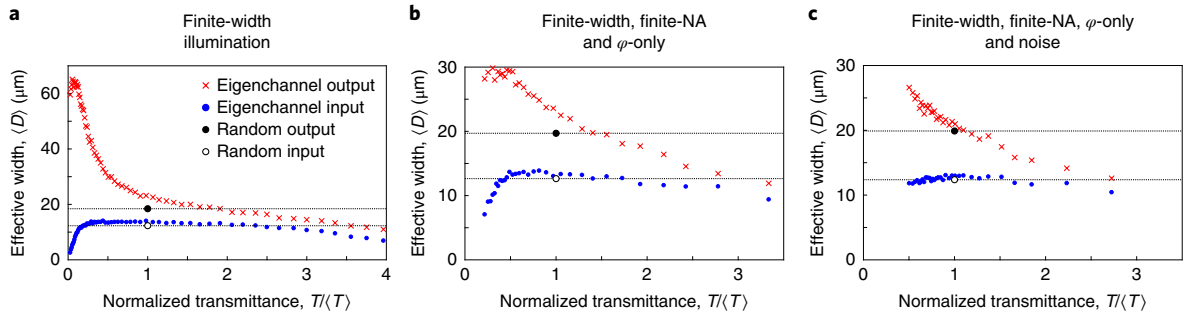

Fig. 5 | Modification of transmission eigenchannel widths by incomplete control. a, Numerically calculated input width (blue circles) and output width (red crosses) of all transmission eigenchannels as a function of the normalized transmittance in 2D diffusive slabs with local illumination. Each data point represents an ensemble average over 50 realizations of disorder. For a random wavefront, the incident beam width at the front surface of the slab is $D_{in}^{rand} \approx 13\,\mu m$ (black open circle), and the transmitted beam width at the back surface is $D_{out}^{rand} \approx 19\,\mu m$ (filled black circle). **b**, Including finite NA for illumination and detection, as well as phase-only (φ-only) modulation of the incident wavefront, reduces the range of eigenchannel widths. **c**, Adding random Gaussian noise to the transmission matrix further modifies the eigenchannel widths, especially for the low-transmission channels. The slab width is $W = 508\,\mu m$, the thickness is $L = 10\,\mu m$, the transport mean free path is $l_t = 1\,\mu m$ and the average refractive index is $n_0 = 1.4$. The slab is sandwiched between air (refractive index $n_1 = 1.0$) and glass (refractive index $n_2 = 1.5$). The calculated input and output intensity profiles for high- and low-transmission eigenchannels in Supplementary Fig. 9 agree well with the experimental data in Fig. 4h,i.

More complex behaviours emerge when we examine eigenchannels with lower transmittance. In our experiment, the low-transmission eigenchannels have incident profiles (Fig. 4f) comparable in size to those of random wavefronts, but with enhanced lateral spreading that leads to wider output profiles (Fig. 4g).

For a more detailed look at the spatial profiles, in Fig. 4h,i we plot the radial intensity profiles for random wavefronts, high-transmission and low-transmission channels at the input and output surfaces, after azimuthal averaging and ensemble averaging. The random wavefronts exhibit sinc^2 profiles on the front surface (see Supplementary Fig. 2 for more details) and have an exponentially decaying tail with 5 μm decay length at the back surface due to diffusion. In comparison, the high-transmission channels have exponentially decaying tails on both front and back surfaces, with a decay length of 2.6 μm at the front and 4 μm at the back. The exponential decay on the front surface and the enhanced decay rate on the back surface, as well as the transverse confinement ($D_{in}^{high} < D_{in}^{rand}$) and the suppressed lateral spreading ($\Delta D^{high} < \Delta D^{rand}$), are signatures of transverse localization of high-transmission channels[62,63].

Figure 4j shows the input and output widths of all of the 2,048 eigenchannels as a function of the normalized transmittance, and compares them to random incident wavefronts. In contrast to Fig. 1c, the eigenchannel widths reveal systematic dependences on the transmittance, particularly for D_{out}. Figure 4k shows that the transverse spreading increases with decreasing transmittance, with the high-transmission eigenchannels exhibiting suppressed lateral spreading and the low-transmission eigenchannels enhanced spreading. In the next section, we show that these properties are also observed numerically when finite illumination area, phase-only modulation, and measurement noises are taken into account in the simulations.

Effect of incomplete control

There are important differences between the experimental set-up and the ideal scenario considered in Figs. 1 and 3. In our experiment, the illumination beam width on the sample surface is comparable to L. Also, we use phase-only modulation over a fraction of incident angles, and collect a fraction of outgoing angles in one polarization. Such experimental conditions lead to incomplete control, which is known to affect the transmittance of eigenchannels[13,64], and we expect them to also modify the eigenchannel profiles. Experimentally it is not possible to separate the different factors, but we can do so with simulations. Numerically we consider 2D disordered slabs with parameters comparable to the experiment (see the caption of Fig. 5), and the asymptotic open-channel width is $D_\infty \approx 90\,\mu m$. Naturally we do not expect quantitative comparison with the 3D sample in the experiment, but we aim to gain physical insights that do not depend on dimensionality.

We describe finite-width illumination by grouping incident modes into equally spaced intervals of transverse momenta that model the SLM macropixels[13]. For random incident wavefronts, the beam widths as defined by the participation number are $D_{in}^{rand} \approx 13\,\mu m$ on the front and $D_{out}^{rand} \approx 19\,\mu m$ on the back surface. Despite the illumination beam width D_{in}^{rand} being much smaller than the asymptotic eigenchannel width D_∞, both high-transmission and low-transmission channels have input widths even smaller than D_{in}^{rand} (Fig. 5a). We attribute this to the fact that these channels utilize multipath interference to enhance or suppress the transmittance. Indeed, crossings of scattering paths inside the sample lead to non-local correlations[52,60] and enhance the range of transmission eigenvalues[13]. Therefore, eigenchannels with extremal eigenvalues prefer smaller input beam widths to increase the probability of crossing. In addition, the extremal eigenchannels preferentially enhance or suppress the intensity near the centre of the transmitted beam (Supplementary Fig. 11). Such a non-uniform modification of the transmitted intensity profile results in an effective reduction of the participation number D_{out} for the high-transmission eigenchannels that we observe in Fig. 5a, and similarly for the increased D_{out} of the low-transmission eigenchannels. We find that the other sources of incomplete control have relatively minor effects. In Fig. 5b we include the phase-only modulation of the incident wavefront, as well as the finite ranges of incident and collecting angles, which are set by the experimental NA in illumination and detection (see Supplementary Section 2.7 for details). The ranges of transmittance and the width of the eigenchannels both decrease, but the qualitative trends remain the same.

Finally, we also model the effect of experimental noise (see Supplementary Section 2.7 for details). As shown in Fig. 5c, the low-transmission eigenchannels are more sensitive to noise than the high-transmission channels: the input widths of low-transmission channels approach those of random incident wavefronts, while the input widths of the high-transmission channels only change slightly. The transverse spreads ΔD of all eigenchannels are plotted in Supplementary Fig. 10. These results agree qualitatively with our experimental data.

Conclusion

In summary, we have discovered transverse localization of transmission eigenchannels in diffusive slabs. In the presence of complete control, each eigenchannel has statistically identical input and output widths as a result of optical reciprocity. In a 2D slab, the asymptotic width for open channels is $D_\infty \approx (2/3)kl_tL$, due to the bandedness and non-local correlations of the real-space transmission matrix. Experimentally, with a finite illumination area, we observe signatures of transverse localization including enhanced lateral confinement, suppressed spreading and exponentially decaying tails for high-transmission channels. The transverse localization results from wave interference effects, which are enhanced by non-local correlations. Due to the reduced illumination area and suppressed lateral spreading, a high-transmission channel is confined into a volume significantly smaller than that from a random wavefront, leading to a significant enhancement of optical energy density that is important for light–matter interactions, imaging and optogenetics in scattering media.

Online content

Any methods, additional references, Nature Research reporting summaries, source data, statements of data availability and associated accession codes are available at https://doi.org/10.1038/s41566-019-0367-9.

Received: 4 June 2018; Accepted: 23 January 2019;
Published online: 04 March 2019

References

1. Dorokhov, O. N. On the coexistence of localized and extended electronic states in the metallic phase. *Solid State Commun.* **51**, 381–384 (1984).
2. Imry, Y. Active transmission channels and universal conductance fluctuations. *Europhys. Lett.* **1**, 249–256 (1986).
3. Mello, P. A., Pereyra, P. & Kumar, N. Macroscopic approach to multichannel disordered conductors. *Ann. Phys.* **181**, 290–317 (1988).
4. Nazarov, Y. V. Limits of universality in disordered conductors. *Phys. Rev. Lett.* **73**, 134–137 (1994).
5. Mosk, A. P., Lagendijk, A., Lerosey, G. & Fink, M. Controlling waves in space and time for imaging and focusing in complex media. *Nat. Photon.* **6**, 283–292 (2012).
6. Vellekoop, I. M. Feedback-based wavefront shaping. *Opt. Express* **23**, 12189–12206 (2015).
7. Rotter, S. & Gigan, S. Light fields in complex media: mesoscopic scattering meets wave control. *Rev. Mod. Phys.* **89**, 015005 (2017).
8. Vellekoop, I. M. & Mosk, A. P. Universal optimal transmission of light through disordered materials. *Phys. Rev. Lett.* **101**, 120601 (2008).
9. Kim, M. et al. Maximal energy transport through disordered media with the implementation of transmission eigenchannels. *Nat. Photon.* **6**, 581–585 (2012).
10. Kim, M., Choi, W., Yoon, C., Kim, G. H. & Choi, W. Relation between transmission eigenchannels and single-channel optimizing modes in a disordered medium. *Opt. Lett.* **38**, 2994–2996 (2013).
11. Popoff, S. M., Goetschy, A., Liew, S. F., Stone, A. D. & Cao, H. Coherent control of total transmission of light through disordered media. *Phys. Rev. Lett.* **112**, 133903 (2014).
12. Bosch, J., Goorden, S. A. & Mosk, A. P. Frequency width of open channels in multiple scattering media. *Opt. Express* **24**, 26472–26478 (2016).
13. Hsu, C. W., Liew, S. F., Goetschy, A., Cao, H. & Stone, A. D. Correlation-enhanced control of wave focusing in disordered media. *Nat. Phys.* **13**, 497–502 (2017).
14. Sarma, R., Yamilov, A. G., Petrenko, S., Bromberg, Y. & Cao, H. Control of energy density inside a disordered medium by coupling to open or closed channels. *Phys. Rev. Lett.* **117**, 086803 (2016).
15. Choi, W., Mosk, A. P., Park, Q.-H. & Choi, W. Transmission eigenchannels in a disordered medium. *Phys. Rev. B* **83**, 134207 (2011).
16. Gérardin, B., Laurent, J., Derode, A., Prada, C. & Aubry, A. Full transmission and reflection of waves propagating through a maze of disorder. *Phys. Rev. Lett.* **113**, 173901 (2014).
17. Davy, M., Shi, Z., Park, J., Tian, C. & Genack, A. Z. Universal structure of transmission eigenchannels inside opaque media. *Nat. Commun.* **6**, 6893 (2015).
18. Ojambati, O. S., Yılmaz, H., Lagendijk, A., Mosk, A. P. & Vos, W. L. Coupling of energy into the fundamental diffusion mode of a complex nanophotonic medium. *New J. Phys.* **18**, 043032 (2016).
19. Koirala, M., Sarma, R., Cao, H. & Yamilov, A. Inverse design of perfectly transmitting eigenchannels in scattering media. *Phys. Rev. B* **96**, 054209 (2017).
20. Hong, P., Ojambati, O. S., Lagendijk, A., Mosk, A. P. & Vos, W. L. Three-dimensional spatially resolved optical energy density enhanced by wavefront shaping. *Optica* **5**, 844–849 (2018).
21. Pendry, J. B. Quasi-extended electron states in strongly disordered systems. *J. Phys. C* **20**, 733 (1987).
22. Bertolotti, J., Gottardo, S., Wiersma, D. S., Ghulinyan, M. & Pavesi, L. Optical necklace states in Anderson localized 1D systems. *Phys. Rev. Lett.* **94**, 113903 (2005).
23. Sebbah, P., Hu, B., Klosner, J. M. & Genack, A. Z. Extended quasimodes within nominally localized random waveguides. *Phys. Rev. Lett.* **96**, 183902 (2006).
24. Choi, W., Park, Q.-H. & Choi, W. Perfect transmission through Anderson localized systems mediated by a cluster of localized modes. *Opt. Express* **20**, 20721–20729 (2012).
25. Peña, A., Girschik, A., Libisch, F., Rotter, S. & Chabanov, A. A. The single-channel regime of transport through random media. *Nat. Commun.* **5**, 3488 (2014).
26. Leseur, O., Pierrat, R., Sáenz, J. J. & Carminati, R. Probing two-dimensional Anderson localization without statistics. *Phys. Rev. A* **90**, 053827 (2014).
27. Skipetrov, S. E. & Page, J. H. Red light for Anderson localization. *New J. Phys.* **18**, 021001 (2016).
28. De Raedt, H., Lagendijk, A. & de Vries, P. Transverse localization of light. *Phys. Rev. Lett.* **62**, 47–50 (1989).
29. Schwartz, T., Bartal, G., Fishman, S. & Segev, M. Transport and Anderson localization in disordered two-dimensional photonic lattices. *Nature* **446**, 52–55 (2007).
30. Karbasi, S. et al. Observation of transverse Anderson localization in an optical fiber. *Opt. Lett.* **37**, 2304–2306 (2012).
31. Hsieh, P. et al. Photon transport enhanced by transverse Anderson localization in disordered superlattices. *Nat. Phys.* **11**, 268–274 (2015).
32. Hu, H., Strybulevych, A., Page, J. H., Skipetrov, S. E. & Van Tiggelen, B. A. Localization of ultrasound in a three-dimensional elastic network. *Nat. Phys.* **4**, 945–948 (2008).
33. Cherroret, N., Skipetrov, S. E. & Van Tiggelen, B. A. Transverse confinement of waves in three-dimensional random media. *Phys. Rev. E* **82**, 056603 (2010).
34. Horstmeyer, R., Ruan, H. & Yang, C. Guidestar-assisted wavefront-shaping methods for focusing light into biological tissue. *Nat. Photon.* **9**, 563–571 (2015).
35. Kim, M., Choi, W., Choi, Y., Yoon, C. & Choi, W. Transmission matrix of a scattering medium and its applications in biophotonics. *Opt. Express* **23**, 12648–12668 (2015).
36. Yu, H. et al. Recent advances in wavefront shaping techniques for biomedical applications. *Curr. Appl. Phys.* **15**, 632–641 (2015).
37. Vynck, K., Burresi, M., Riboli, F. & Wiersma, D. S. Photon management in two-dimensional disordered media. *Nat. Mater.* **11**, 1017–1022 (2012).
38. Liew, S. F. et al. Coherent control of photocurrent in a strongly scattering photoelectrochemical system. *ACS Photon.* **3**, 449–455 (2016).
39. Baranger, H. U., DiVincenzo, D. P., Jalabert, R. A. & Stone, A. D. Classical and quantum ballistic-transport anomalies in microjunctions. *Phys. Rev. B* **44**, 10637–10675 (1991).
40. Jalas, D. et al. What is—and what is not—an optical isolator. *Nat. Photon.* **7**, 579–582 (2013).
41. Freund, I., Rosenbluh, M. & Feng, S. Memory effects in propagation of optical waves through disordered media. *Phys. Rev. Lett.* **61**, 2328–2331 (1988).
42. Berkovits, R., Kaveh, M. & Feng, S. Memory effect of waves in disordered systems: a real-space approach. *Phys. Rev. B* **40**, 737–740 (1989).
43. Judkewitz, B., Horstmeyer, R., Vellekoop, I. M., Papadopoulos, I. N. & Yang, C. Translation correlations in anisotropically scattering media. *Nat. Phys.* **11**, 684–689 (2015).
44. Osnabrugge, G., Horstmeyer, R., Papadopoulos, I. N., Judkewitz, B. & Vellekoop, I. M. Generalized optical memory effect. *Optica* **4**, 886–892 (2017).
45. Casati, G., Molinari, L. & Izrailev, F. Scaling properties of band random matrices. *Phys. Rev. Lett.* **64**, 1851–1854 (1990).
46. Izrailev, F. M. Simple models of quantum chaos: spectrum and eigenfunctions. *Phys. Rep.* **196**, 299–392 (1990).
47. Fyodorov, Y. V. & Mirlin, A. D. Analytical derivation of the scaling law for the inverse participation ratio in quasi-one-dimensional disordered systems. *Phys. Rev. Lett.* **69**, 1093–1096 (1992).
48. Stephen, M. J. & Cwilich, G. Intensity correlation functions and fluctuations in light scattered from a random medium. *Phys. Rev. Lett.* **59**, 285–287 (1987).
49. Feng, S., Kane, C., Lee, P. A. & Stone, A. D. Correlations and fluctuations of coherent wave transmission through disordered media. *Phys. Rev. Lett.* **61**, 834–837 (1988).

50. Mello, P. A., Akkermans, E. & Shapiro, B. Macroscopic approach to correlations in the electronic transmission and reflection from disordered conductors. *Phys. Rev. Lett.* **61**, 459–462 (1988).
51. Pnini, R. & Shapiro, B. Fluctuations in transmission of waves through disordered slabs. *Phys. Rev. B* **39**, 6986–6994 (1989).
52. Berkovits, R. & Feng, S. Correlations in coherent multiple scattering. *Phys. Rep.* **238**, 135–172 (1994).
53. Genack, A. Z., Garcia, N. & Polkosnik, W. Long-range intensity correlation in random media. *Phys. Rev. Lett.* **65**, 2129–2132 (1990).
54. Scheffold, F., Härtl, W., Maret, G. & Matijevíc, E. Observation of long-range correlations in temporal intensity fluctuations of light. *Phys. Rev. B* **56**, 10942–10952 (1997).
55. Sebbah, P., Hu, B., Genack, A. Z., Pnini, R. & Shapiro, B. Spatial-field correlation: the building block of mesoscopic fluctuations. *Phys. Rev. Lett.* **88**, 123901 (2002).
56. Yamilov, A. Relation between channel and spatial mesoscopic correlations in volume-disordered waveguides. *Phys. Rev. B* **78**, 045104 (2008).
57. Strudley, T., Zehender, T., Blejean, C., Bakkers, E. P. A. M. & Muskens, O. Mesoscopic light transport by very strong collective multiple scattering in nanowire mats. *Nat. Photon.* **7**, 413–418 (2013).
58. Fayard, N., Cazé, A., Pierrat, R. & Carminati, R. Intensity correlations between reflected and transmitted speckle patterns. *Phys. Rev. A* **92**, 033827 (2015).
59. Starshynov, I. et al. Non-Gaussian correlations between reflected and transmitted intensity patterns emerging from opaque disordered media. *Phys. Rev. X* **8**, 021041 (2018).
60. Akkermans, E. & Montambaux, G. *Mesoscopic Physics of Electrons and Photons* (Cambridge Univ. Press, Cambridge, 2007).
61. Popoff, S. M. et al. Measuring the transmission matrix in optics: an approach to the study and control of light propagation in disordered media. *Phys. Rev. Lett.* **104**, 100601 (2010).
62. Sheng, P. *Introduction to Wave Scattering, Localization and Mesoscopic Phenomena* (Academic Press, San Diego, CA, 1995).
63. Kramer, B. & MacKinnon, A. Localization: theory and experiment. *Rep. Prog. Phys.* **56**, 1469–1564 (1993).
64. Goetschy, A. & Stone, A. D. Filtering random matrices: the effect of incomplete channel control in multiple scattering. *Phys. Rev. Lett.* **111**, 063901 (2013).

Acknowledgements

We thank A. Mosk, A. Genack, B. Shapiro, F. Scheffold, S. Skipetrov, S. Bittner, S. Rotter and T. Kottos for stimulating discussions and useful feedback. We acknowledge financial support by the Office of Naval Research (ONR) under grant no. MURI N00014-13-0649 and by the US–Israel Binational Science Foundation (BSF) under grant no. 2015509, as well as computational resources provided by the Yale High Performance Computing Cluster (Yale HPC).

Author contributions

H.Y. performed the experiments and analysed the data. C.W.H. performed the numerical simulations and fabricated the samples. H.Y. analysed the numerical data. C.W.H. helped with experimental data acquisition and contributed to numerical data analysis. H.C. supervised the project. All authors contributed to the interpretation of the results. H.Y. and C.W.H. prepared the manuscript, H.C. edited it and A.Y. provided feedback.

Competing interests

The authors declare no competing interests.

Additional information

Supplementary information is available for this paper at https://doi.org/10.1038/s41566-019-0367-9.

Reprints and permissions information is available at www.nature.com/reprints.

Correspondence and requests for materials should be addressed to H.C.

Publisher's note: Springer Nature remains neutral with regard to jurisdictional claims in published maps and institutional affiliations.

Methods

Numerical simulation of transmission eigenchannels. We solve the 2D scalar wave equation $[\nabla^2 + k_0^2\epsilon(\mathbf{r})]\psi(\mathbf{r}) = 0$ on a finite-difference grid, where k_0 is the vacuum wavenumber, $\epsilon(\mathbf{r})$ the dielectric constant at spatial position $\mathbf{r}$, and $\psi(\mathbf{r})$ the electric field at $\mathbf{r}$. We consider disordered slabs of width W and thickness L in background refractive index n_0. The dielectric constant of the slab is modelled as $\epsilon(\mathbf{r}) = n_0^2 + \delta\epsilon(\mathbf{r})$ at each grid point, and $\delta\epsilon(\mathbf{r})$ is a random number drawn from a zero-mean uniform distribution whose width determines the transport mean free paths l_t (see Supplementary Section 2.1 for details). After calculating the field transmission matrix t for the entire slab using the recursive Green's function method[39], we obtain the incident wavefront V_n of an eigenchannel via $t^\dagger t V_n = \tau_n V_n$, and calculate its spatial profile with such an incident wavefront. In this work we focus on scattering systems in the diffusive regime of transport, namely $Nl_t \gg L \gg l_t$, where $N \approx kW/\pi$ is the number of modes.

Participation number. The lateral width of an eigenchannel is given by the participation number of its transverse intensity profile. The input width is found from the expression

$$D_{\mathrm{in}} \equiv \frac{\left[\int_0^W |V_n(x)|^2\,\mathrm{d}x\right]^2}{\int_0^W |V_n(x)|^4\,\mathrm{d}x}$$

where $V_n(x)$ is the incident field distribution at the input surface obtained from the nth eigenvector of $t^\dagger t$. Similarly, the output width D_{out} of the nth eigenchannel is obtained from the transmitted field distribution $U_n(x)$ at the output surface. For a 2D intensity distribution $I(x,y)$, its effective area A is computed from the 2D participation number:

$$A \equiv \frac{\left[\iint I(x,y)\mathrm{d}x\mathrm{d}y\right]^2}{\iint I^2(x,y)\mathrm{d}x\mathrm{d}y}$$

Data availability

The data that support the plots within this paper and other findings of this study are available from the corresponding author upon reasonable request.

nature photonics

SUPPLEMENTARY INFORMATION

https://doi.org/10.1038/s41566-019-0367-9

In the format provided by the authors and unedited.

Transverse localization of transmission eigenchannels

Hasan Yılmaz[1], Chia Wei Hsu[1], Alexey Yamilov[2] and Hui Cao[1]*

[1]Department of Applied Physics, Yale University, New Haven, CT, USA. [2]Department of Physics, Missouri University of Science & Technology, Rolla, MO, USA. *e-mail: hui.cao@yale.edu

Transverse localization of transmission eigenchannels: supplementary material

Hasan Yılmaz[1], Chia Wei Hsu[1], Alexey Yamilov[2], and Hui Cao[1,*]

[1]Department of Applied Physics, Yale University, New Haven, Connecticut 06520, USA
[2]Department of Physics, Missouri University of Science & Technology, Rolla, Missouri 65409, USA
[*]hui.cao@yale.edu

ABSTRACT

This document provides supplementary information to "Transverse localization of transmission eigenchannels". In the first section we elaborate on the experimental setup and measurement procedure. In the second section, we present details of the numerical simulations.

1 Experiment

The scattering sample in our experiment is made of closely-packed zinc oxide (ZnO) nanoparticles (average diameter $\sim$ 200 nm), deposited on a cover slip of thickness 170 μm. The ZnO layer thickness is about 10 μm, and the transport mean free path is approximately 1.5 μm. The average transmittance is approximately 0.2. We define the interface between ZnO and air as the front (input) surface, and the interface between the ZnO and the cover slip as the back (output) surface of the sample. The effective index of refraction for the ZnO nanoparticle layer is about 1.4, which almost matches the refractive index of the glass substrate (cover slip).

Our experimental setup is sketched in Fig. S1. A linearly-polarized monochromatic laser beam (Coherent, Compass 215M-50 SL) with wavelength $\lambda = 532$ nm is expanded and then clipped in order to uniformly cover a large area on the spatial light modulator (SLM). Its polarization direction is rotated from vertical to 45° by a half-wave ($\lambda/2$) plate, and consequently split into vertical and horizontal polarizations by a polarizing beam splitter (PBS). The horizontal-polarized component of the beam illuminates one part of a reflective phase-only SLM (Hamamatsu, X10468-01). Since the SLM only modulates horizontal polarization, the vertical-polarized component of the beam is converted to horizontal polarization by another $\lambda/2$ plate before impinging onto the second part the SLM; the modulated reflected beam is converted back to vertical polarization after passing through the same $\lambda/2$ plate again. The two polarizations are recombined at the PBS, and the SLM plane is imaged onto the pupil of a microscope objective MO_1 (Nikon CF Plan 100× with a numerical aperture $NA_{in} = 0.95$) by a pair of lenses L_1 and L_2 (with focal lengths $f_1 = f_2 = 200$ mm). This setup enables independent modulation of the spatial wavefront for two orthogonal polarizations. An iris diaphragm ID_1 between L_1 and L_2 blocks high-order diffractions from the SLM. The objective MO_1 projects the Fourier transform of the SLM phase pattern onto the front (input) surface of the scattering sample. The image of the iris diaphragm ID_1 on the sample front surface is approximately a circle with diameter 22.5 μm.

To measure the spatial profile of illumination on the sample surface, we insert a beam splitter before the objective MO_1 to split the input beam, and use another lens L_3 ($f_3 = 100$ mm) to image the Fourier plane of the SLM onto a CCD camera CCD1 (Allied Vision, Guppy PRO F-031B). An iris ID_2 between the beam splitter and L_3 blocks light that does not enter MO_1.

In transmission, the Fourier transform of the transmitted field on the back (output) surface of the sample is imaged onto a CCD camera CCD2 (Allied Vision, Manta G-031B) by an oil-immersion microscope objective MO_2 (Edmund DIN Achromatic 100×, $NA_{out} = 1.25$) and a pair of lens L_4 ($f_4 = 200$ mm) and L_5 ($f_5 = 100$ mm). The field of view of MO_2 on the back surface of the sample has a diameter of 180 μm. A linear polarizer is placed right after MO_2 to filter out one polarization component of the transmitted light. In between the polarizer and the lens L_4, a beam splitter is inserted to split the output beam, and the intensity profile on the back (output) surface of the sample is imaged onto another CCD camera CCD3 (Allied Vision, Pike F-100B) by a lens L_6 ($f_6 = 200$ mm).

Field transmission matrix from the SLM to the CCD2 is measured in Hadamard basis, with a common-path interferometry akin to the method in reference[1]. 3912 SLM macropixels (1956 per polarization) are imaged onto the entrance pupil of MO_1, covering the entire pupil. Among these, we use 2048 macropixels (1024 per polarization) for the signal field and 1864 macropixels for the reference field in the transmission matrix measurement. Each macropixel consists of 4×4 SLM pixels. A random (but fixed) phase pattern is displayed on the reference pixels. In order to measure the transmitted intensity of signal field in each Hadamard basis vector, a high-spatial-frequency phase grating is written to the reference region of the SLM so that the reference field is diffracted away from the iris ID_1.

After measuring the field transmission matrix, we calculate the eigenvectors which represent the input wavefronts for individual transmission eigenchannels:

$$\tilde{t}^\dagger \tilde{t} \tilde{V}_n = \tau_n \tilde{V}_n, \tag{S1}$$

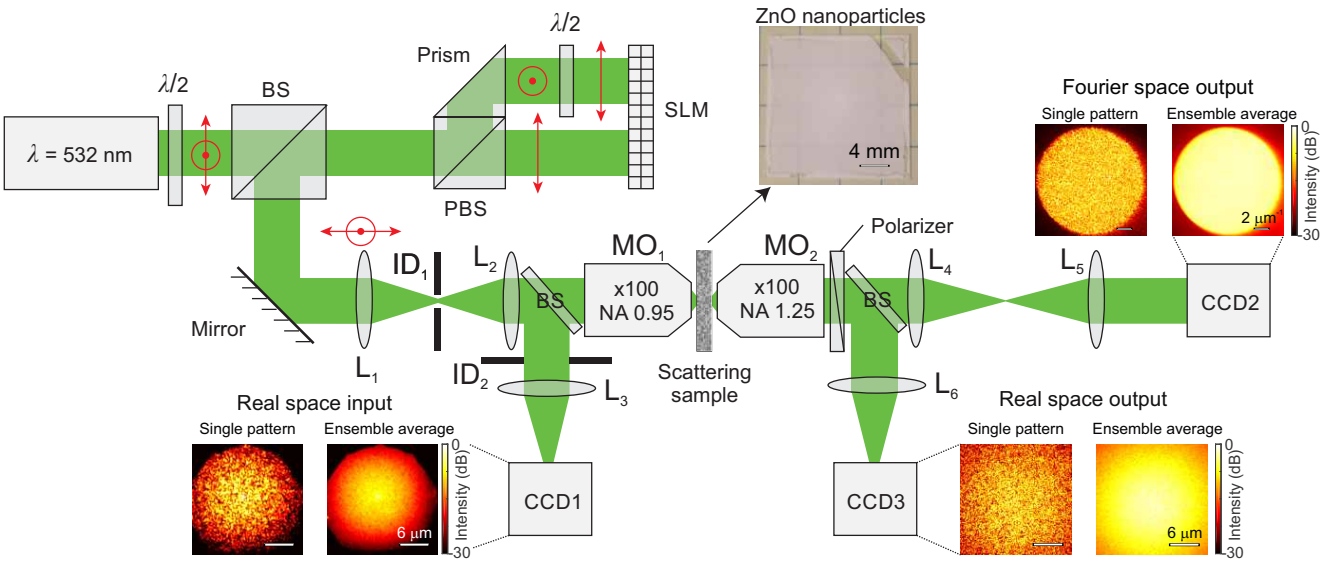

Figure S1. Detailed experimental setup. A reflective phase-only spatial light modulator (SLM) modulates the phase-fronts of orthogonal linear polarization components of a monochromatic laser beam ($\lambda = 532$ nm). The optical field transmission matrix of the scattering sample is measured in k-space with the SLM and the camera CCD2. The scattering sample, shown in the inset, is a 10 μm-thick film of ZnO nanoparticles with average transmittance 0.2, deposited on a glass substrate. Cameras CCD1 and CCD3 image the spatial intensity profiles of light on the front (input) and back (output) surfaces of the sample, respectively. For each camera, the intensity profile of a single measured pattern and that averaged over 50 ensembles are shown as inset. $\lambda/2$, half-wave plate; BS, beam splitter; PBS, polarizing beam splitter; MO_{1-2}, microscope objectives; L_{1-6}, lenses; ID_{1-2}, iris diaphragms.

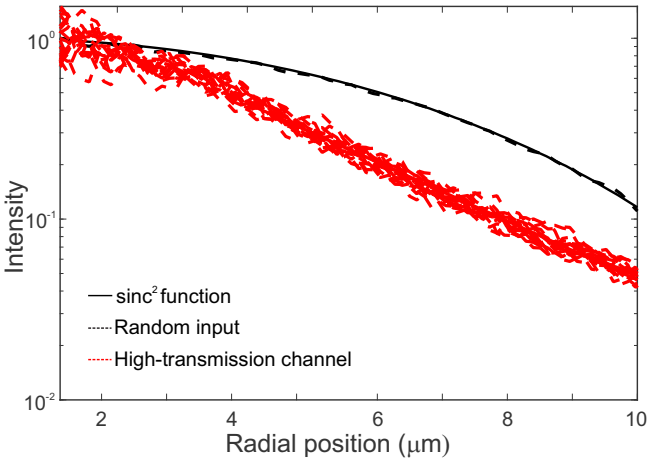

Figure S2. Radial intensity profiles of high-transmission channels and random inputs. Red dashed lines represent azimuthally averaged intensity profiles of 20 highest-transmission eigenchannels that are incident on the front surface of the diffusive ZnO slab. The intensity is normalized to 1 at the origin. All high-transmission channels decay exponentially in radial direction. For comparison, black dashed lines are azimuthally averaged intensity profiles for random incident wavefronts on the front surface of the same slab. They are averaged over 20 random wavefronts to show the envelope. The solid black line is the illumination profile predicted from the SLM macropixel (4×4 pixels): $I^{\mathrm{rand}} = \langle \mathrm{sinc}^2(qx/2) \times \mathrm{sinc}^2(qy/2) \rangle_\theta$, where q is given by the macropixel size on the entrance pupil of illumination objective and $\langle ... \rangle_\theta$ denotes azimuthal average. The sinc^2 profile results from the square shape of SLM macropixel.

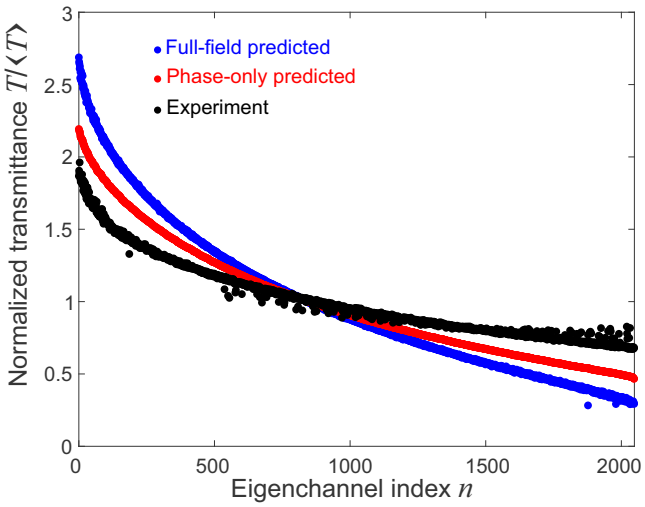

Figure S3. Normalized transmittance $T/\langle T \rangle$ for all eigenchannels. Blue circles represent $T/\langle T \rangle$, predicted from the measured transmission matrix, with both phase and amplitude modulations of incident fields, the red circles with phase-only modulation of input. Black circles denote the experimentally measured $T/\langle T \rangle$ when the phases of input eigenvectors are displayed on the SLM.

where $\tilde{V}_n$ is the n-th eigenvector, and τ_n is the corresponding eigenvalue that gives the transmittance of the n-th eigenchannel. After finding the eigenvectors, we display the phase pattern of $\tilde{V}_n$ on the 2048 macropixels of the SLM, and record the intensity profiles on the front and back surfaces of the scattering sample. At this time, the high-spatial-frequency phase grating is displayed on the reference region of the SLM to block the reference field. Fig. S2 shows radial intensity profiles of 20 highest-transmission channels and compares to random inputs. In contrast to the sinc^2 envelope of random wavefronts incident on the front surface of the slab, the intensity profiles of high-transmission channels decay exponentially in the radial direction.

Fig. S3 shows the measured transmittance T normalized by the mean $\langle T \rangle$ for every eigenchannel in our experiment. The blue and red circles denote the values of $T/\langle T \rangle$ predicted from the measured transmission matrix with full-field modulation and phase-only modulation respectively, and black circles represent the experimentally measured $T/\langle T \rangle$ when phases of eigenvectors $\tilde{V}_n$ are displayed on the SLM. While the range of $T/\langle T \rangle$ is predicted to be between 2.2 and 0.47 in case of phase-only modulation, the experimental values of $T/\langle T \rangle$ range from 1.95 to 0.67 due to sample drift and measurement noises.

2 Numerical simulations

In this section, we present details of our numerical simulations. Subsection 2.1 describes the extraction of transport and scattering mean free paths of the disordered slabs. Subsection 2.2 depicts the relation between sample thickness L and real-space transmission matrix bandwidth b. In subsection 2.3, spatial distribution of centre positions of transmission eigenchannels is shown. Subsection 2.4 narrates how the asymptotic channel widths are obtained in wide slab geometry. In subsection 2.5, a histogram of open channel width and the relation between channel width and exponential decay length are presented. In subsection 2.6, we present a scaling analysis of uncorrelated random banded matrices to illustrate the effects of correlations on eigenchannel localization. Subsection 2.7 provides details of numerical simulations that account for finite-width illumination, finite numerical aperture, phase-only control, and measurement noise in the experiment.

We simulate wave propagation through two-dimensional (2D) diffusive slabs numerically. The normalized width of a slab is $k_0 W$ and the normalized thickness is $k_0 L$, where $k_0 = 2\pi/\lambda$ and λ is the vacuum wavelength. The slab is discretized on a 2D square grid, and the grid size is $(\lambda/2\pi) \times (\lambda/2\pi)$. The dielectric constant at each grid point is $\varepsilon(\mathbf{r}) = n_0^2 + \delta\varepsilon(\mathbf{r})$, where n_0 is the average refractive index of the disordered slab, $\delta\varepsilon(\mathbf{r})$ a random number drawn from the interval $[-\sigma, \sigma]$ with uniform probability. The disordered slab is sandwiched between two homogeneous materials with refractive indices of n_1 and n_2. Either perfectly reflecting (Dirichlet) or periodic boundary conditions are applied to the transverse boundaries.

To obtain the field transmission matrix t at wavelength λ, we solve the scalar wave equation $\left[\nabla^2 + k_0^2 \varepsilon(\mathbf{r})\right] \psi(\mathbf{r}) = 0$ with the recursive Green's function method[2]. The singular value decompostion of $t = U\sqrt{\tau}V^\dagger$ gives the transmission eigenvalue τ, the input V and output U wavefronts of transmission eigenchannels.

2.1 Extraction of transport and scattering mean free paths

In this and the following five subsections, the average refractive indices of the disordered slabs match those of the surroundings, $n_0 = n_1 = n_2$, and the perfectly reflecting (Dirichlet) boundary conditions are applied to the transverse boundaries. In this subsection, we set $n_0 = n_1 = n_2 = 1.5$. The transport mean free path l_t is obtained from the average transmittance $\langle T \rangle$:

$$\langle T \rangle = \frac{(1+\Delta)\, l_t}{L + 2\Delta l_t}, \tag{S2}$$

where $\Delta = 0.818$ for the 2D diffusive slab with index-matched homogeneous media at both surfaces[3,4].

To extract scattering mean free path l_s for a fixed strength of disorder σ, we calculate the transmission matrices of waveguides with the same width $k_0 W = 100$ and varying thickness between $k_0 L = 1$ and $k_0 L = 6 k_0 l_t$. After average over 40000 disorder realizations, the diagonal elements of the transmission matrices $\langle t_{ii} \rangle$ give the scattering mean free path[5]

$$|\langle t_{ii} \rangle|^2 = \exp\left[\frac{-kL}{k_{z,i} l_s}\right], \tag{S3}$$

where $k_{z,i}$ the longitudinal component of the wave vector for each waveguide mode i. Table S1 presents the values of the transport mean free path and the scattering mean free path for different strengths of disorder σ. Their values are approximately equal, $l_t \approx l_s$.

Table S1. Transport mean free path l_t and scattering mean free path l_s for each disorder strength σ.

σ	0.60	0.65	0.75	0.90	1.10	1.45
kl_t	30.9	27.1	19.3	13.5	8.7	4.6
kl_s	34.3	29.3	22.2	15.5	10.4	6.0

2.2 Bandwidth b of real-space transmission matrices

We compute the bandwidth b of real-space transmission matrices using the definition of the participation number

$$b \equiv \left\langle \frac{\left[\sum_i |\, t_{ij}\,|^2\right]^2}{\sum_i |\, t_{ij}\,|^4} \right\rangle, \tag{S4}$$

where $\langle ... \rangle$ denotes averaging over all columns j of the real-space transmission matrices for 10 different realizations of disorder. We observe the bandwidth b of the real-space transmission matrix scales linearly with the slab thickness L, as shown in Fig. S4. The linear scaling confirms diffusive transport in the 2D disordered slabs.

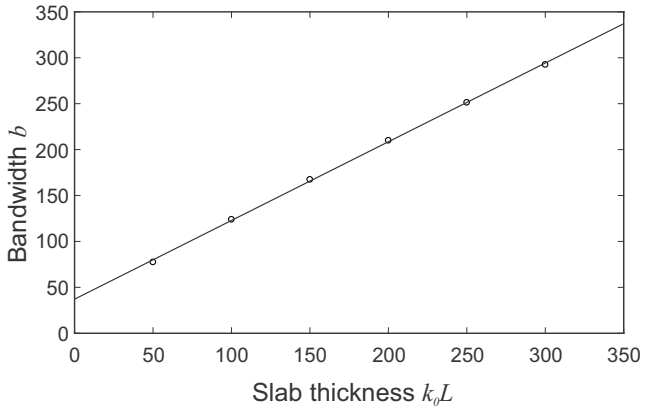

Figure S4. Bandwidth b of real-space transmission matrices versus the slab thickness k_0L. Black open circles and black solid line indicate numerical data and a linear regression, respectively. The slab width is $k_0W = 6000$. The transport mean free path is $kl_t = 19.3$. The linear scaling of bandwidth b with the slab thickness L is a result of diffusive transport.

2.3 Spatial distribution of transmission eigenchannels

With the transmission matrix, we calculated the field distribution of each eigenchannel at the front and back surfaces of the slab. To find the centre position of the lateral intensity profile of each channel, we computed its centre of mass in the transverse direction x,

$$x_0 = \frac{\int_{-W/2}^{W/2} |\psi_n(x)|^2 x \mathrm{d}x}{\int_{-W/2}^{W/2} |\psi_n(x)|^2 \mathrm{d}x}, \tag{S5}$$

where $\psi_n(x) = V_n(x), U_n(x)$ at the front and back sides. We plot the centre positions x_0/W of all transmission eigenchannels in Fig. S5. For every channel, the centre position at the front surface coincides with that at the back surface of the slab. Transmission eigenchannels are randomly and homogeneously distributed across the entire slab independent of their eigenvalues τ_n.

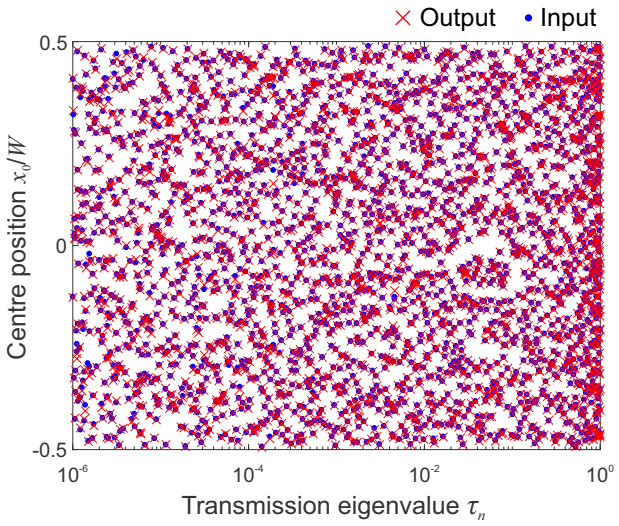

Figure S5. Centre positions of transmission eigenchannels. The centre of mass x_0/W of all transmission eigenchannels on the front and back surfaces of a diffusive slab are plotted with blue filled circles and red crosses, respectively. Transmission eigenchannels are located randomly and homogeneously across the entire slab regardless of their eigenvalues τ_n. Sample parameters: $k_0W = 6000$, $k_0L = 50$, $kl_t = 4.6$.

2.4 Asymptotic widths of open channels

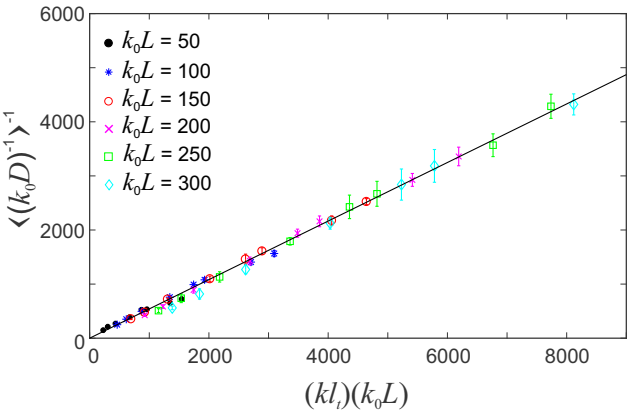

Figure S6. Scaling of asymptotic width D_∞ of transmission eigenchannels. k_0D_∞ is obtained from $\langle (k_0D)^{-1} \rangle^{-1}$ in the limit $W \to \infty$. D_∞ of diffusive slabs with different L, l_t, and n_0, showing a universal scaling $D_\infty \propto (n_0k_0l_t)L$. Linear regression gives the proportionality constant to be 0.54 (black solid line). Each data point represents an ensemble average over all open channels (with $\tau_n \geq 1/\mathrm{e}$) in 10 realizations of disorder; the error bars are the standard deviation among the disorder realizations.

We excited a single open channel and calculated its input and output widths from the participation numbers of field intensity distributions on the front and back surfaces of the slab. We

repeat this calculation for slabs of different widths $k_0W =$ 100, 250, 500, 1000, 2000, 3000, 4500, 6000, while fixing the thickness k_0L, the average refractive index $n_0 = n_1 = n_2$, and the strength of disorder σ. The channel widths are averaged over all open channels with transmission eigenvalue $\tau_n \geq 1/\mathrm{e}$.

As shown in Fig. 1b of the main text, as the slab width W increases, the open channel width k_0D first increases, then saturates to a constant value, which can be extracted from a two-parameter fit,

$$\langle k_0 D \rangle = \left(a_0 + \frac{a_1}{k_0 W} \right)^{-1}. \tag{S6}$$

The asymptotic open channel width $k_0D_\infty = 1/a_0$ is obtained in the limit $W \to \infty$.

We apply the above procedure to slabs of different thickness $k_0L = 50, 100, 150, 200, 250, 300$ to find the scaling of D_∞ with L, while fixing n_0 and σ. To find the scaling of D_∞ with l_t, the disorder strength in the slab is varied as $\sigma = 0.6$, 0.65, 0.75, 0.9, 1.1, 1.45. The corresponding normalized transport mean free paths kl_t are given in table S1. For each set of parameters (k_0L, σ, k_0W), we simulate 10 different realizations of disorder to obtain the ensemble-averaged values. In addition to $n_0 = n_1 = n_2 = 1.5$, we also set $n_0 = n_1 = n_2 = 1$, then vary the thickness k_0L (as listed above) and $\sigma = 0.6$, 1.1 ($kl_t = 17.4, 6.1$). To check whether the transverse boundary conditions affect the channel widths, we repeat the simulations with periodic boundary conditions, and obtain the same asymptotic open channel widths shown in Fig. 3 of the main text.

Next, we examine whether the scaling of D_∞ depends on the way of averaging. Instead of obtaining D_∞ from $\langle D \rangle$ in the limit of $W \to \infty$, we compute $\langle 1/D \rangle$ and extract D_∞ from its inverse in $W \to \infty$ limit. The same scaling of $D_\infty \propto kl_tL$ is obtained, as shown in Fig. S6, only the prefactor of 0.54 is slightly different from that of 0.68 in Fig. 3c of the main text.

2.5 Channel width versus decay length

We investigate the probability density function (PDF) of open channel widths. Fig. S7a is a histogram of normalized width $D/\langle D \rangle$. The channel width D fluctuates around the mean $\langle D \rangle$. The standard deviation of $D/\langle D \rangle$ is 0.24.

As shown in Fig. S2, all open channels exhibit an exponential decay in the transverse direction. To find the decay lengths of open channels (with $\tau_n \geq 1/\mathrm{e}$), we average the lateral intensity profiles corresponding to the same eigenvalue index over 10 disorder realizations after shifting each profile's centre of mass to the origin of transverse coordinate. We fit the tail with an exponential function to obtain the decay length ξ.

To find the relation between the decay length ξ and the lateral width D of open channels, we plot ξ and D for all open channels in Fig S7b. The narrower channels tend to decay faster. The Pearson coefficient between $D/\langle D \rangle$ and $\xi/\langle \xi \rangle$ is 0.8, indicating that the channel width is proportional to the decay length.

2.6 Uncorrelated banded random matrices

To illustrate the effects of correlations in transmission matrices on eigenchannel widths, we built banded random matrices of uncorrelated matrix elements. First, we generate a square matrix of uncorrelated complex circular Gaussian random numbers with a size of $k_0W \times k_0W$. Then, we multiply the amplitudes of the matrix elements with a function $f(x)$ to introduce a diagonal band to the matrix. $f(x)$ represents the field amplitude on the back surface of a slab for a delta source on the front surface. It is given by the solution of 2D steady-state diffusion equation[6]:

$$f(x) = \frac{1}{\cosh(\pi x/2L)}, \tag{S7}$$

where x denotes the transverse spatial coordinate and L is the slab thickness. This amplitude profile agrees with the amplitude envelope of the real-space transmission matrices calculated by recursive Green's function method.

We constructed uncorrelated banded random matrices for $k_0W = 100$, 250, 500, 1000, 2000, 3000, 4500, and 6000 of each with $k_0L = 5$, 10, 15, 20, 25, 30, 50, and 100 (10 disorder realizations for every combination of k_0W and k_0L, in total 640 matrices). We computed eigenvectors of $t^\dagger t$ and corresponding effective eigenvector widths using the participation number. In Fig S8, we show examples of a transmission (correlated) matrix (a), an uncorrelated random matrix (c) with same bandwidth $b = k_0L = 100$ and their eigenvector profiles (b,d). The eigenvector of the correlated banded matrix is transversely localized. In contrast, the eigenvector profile for the uncorrelated banded matrix is not localized but occupies the entire width of the system.

In order to show the scaling of asymptotic eigenvector width of uncorrelated banded random matrices, we performed the same scaling analysis that we did for transmission matrices to extrapolate asymptotic eigenvector widths. Similar to the averaging we performed for the transmission eigenchannel widths, we averaged over eigenvector widths for the eigenvectors with $\tau_n/\tau^{\max} \geq 1/\mathrm{e}$ of 10 different matrix realizations. Fig. S8e is a log-log plot of the asymptotic eigenvector widths versus the slab thickness k_0L for the (correlated) transmission matrices and the uncorrelated random banded matrices. A least-squares regression gives a scaling of $D_\infty \propto L^2$ for the uncorrelated random banded matrices as expected from banded random matrix theory[7–9]. In stark contrast, we observe $D_\infty \propto L$ scaling for the correlated transmission matrices.

2.7 Incomplete control

Experimentally only a small region of a wide slab is illuminated, and partial transmission matrix is measured. We numerically investigate the effects of finite-width illumination, finite numerical aperture (NA), phase-only modulation, and noise on the spatial profiles of transmission eigenchannels.

We first calculate the complete transmission matrices of 2D slabs for 50 disorder realizations. The slab parameters,

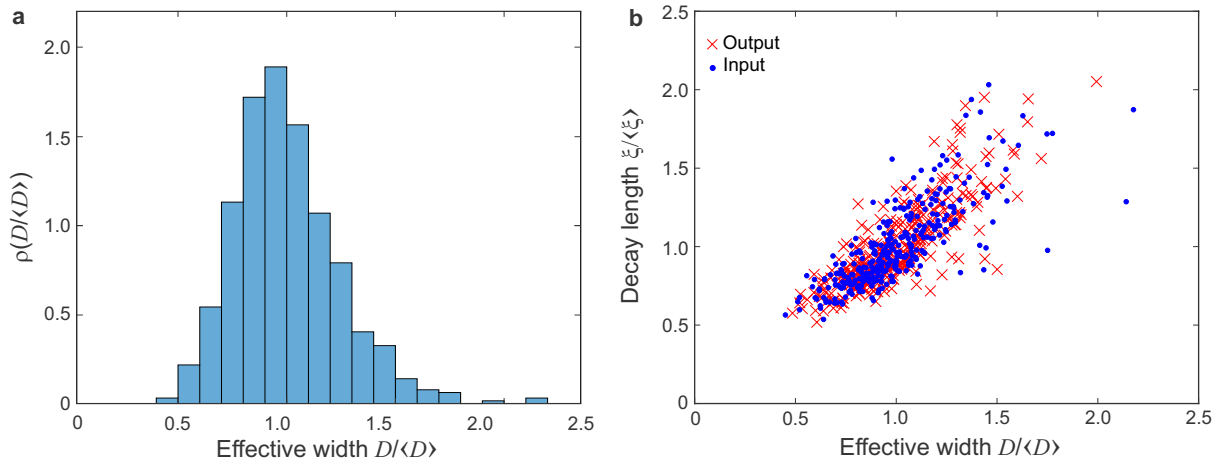

Figure S7. Open channel width and decay length. a, Histogram of lateral width D of open channels, normalized by the mean $\langle D\rangle$. The standard deviation of $D/\langle D\rangle$ is 0.24. **b**, Scatter plot of lateral width $D/\langle D\rangle$ versus decay length $\xi/\langle\xi\rangle$ of all open channels. The Pearson correlation coefficient between them is 0.8, indicating a linear relation. The slab parameters are the same as those in Fig. S5.

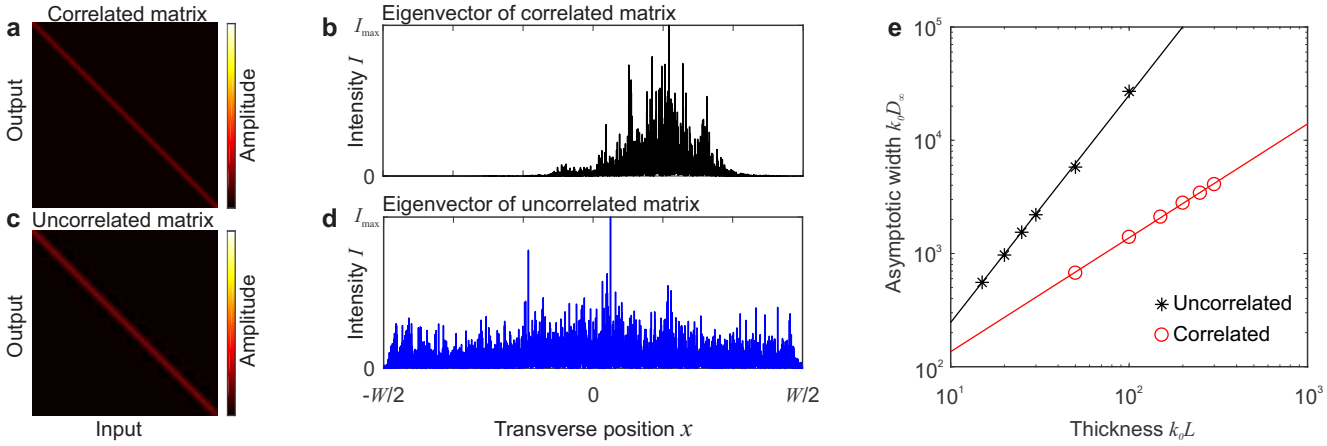

Figure S8. Correlated and uncorrelated banded random matrices. a, Amplitude of the real-space transmission matrix obtained from recursive Green's function method. Parameters: $k_0 W = 6000$, $k_0 L = 100$, and $k l_t = 19.3$. **b**, Spatial intensity profile of an eigenchannel of the transmission matrix in (a), showing transverse localization. **c**, Amplitude of a banded random matrix with uncorrelated matrix elements. Matrix dimension and bandwidth are identical to (a). **d**, Spatial intensity profile of an eigenvector of the matrix in (c), extending over the entire width of the system. Both eigenvectors have eigenvalues of τ_n = 0.67. **e**, Black asterisks represent asymptotic width of eigenvectors of uncorrelated banded random matrix, which exhibits a scaling $D_\infty \propto L^2$, as expected from banded random matrix theory. Red circles represent asymptotic width of eigenchannels of correlated transmission matrices, which exhibits a scaling $D_\infty \propto L$.

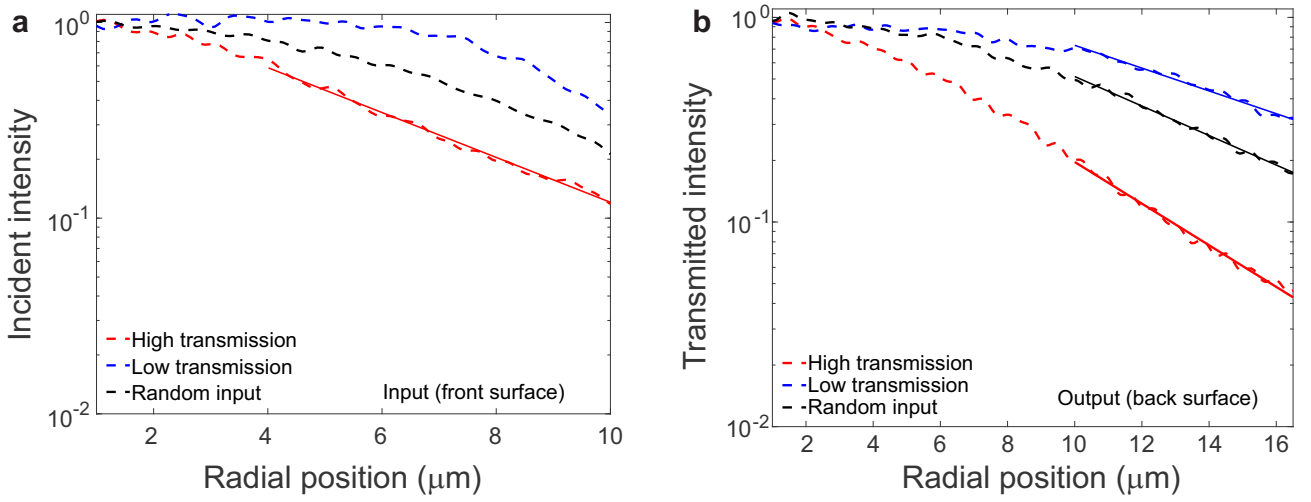

Figure S9. Calculated spatial profiles of high and low-transmission channels with finite-width illumination. Normalized radial intensity profiles of random incident wavefronts (black), high-transmission (red), and low-transmission (blue) channels on the front (a) and the back (b) surfaces of the sample. The illumination beam diameter is ~20 μm. Dashed lines are calculated intensities averaged azimuthally and over 50 disorder realizations. At the front surface, the intensity profile of high-transmission channels decays exponentially at the tail ($r = 4$ μm to 10 μm), with a decay length of 3.8 μm (red solid line), while the random input profiles follow a sinc^2 function (black dashed line). On the back side, both high and low transmission channels feature exponential tails, so as the random input wavefronts. The solid lines represent exponential fits of the tails ($r =$ 10 μm to 16 μm), giving the decay length of 4.3 μm for high-transmission channels, 7.8 μm for low-transmission channels, and 6 μm for the random incident wavefronts. The sample parameters in numerical simulations are same as in Figs. 5.

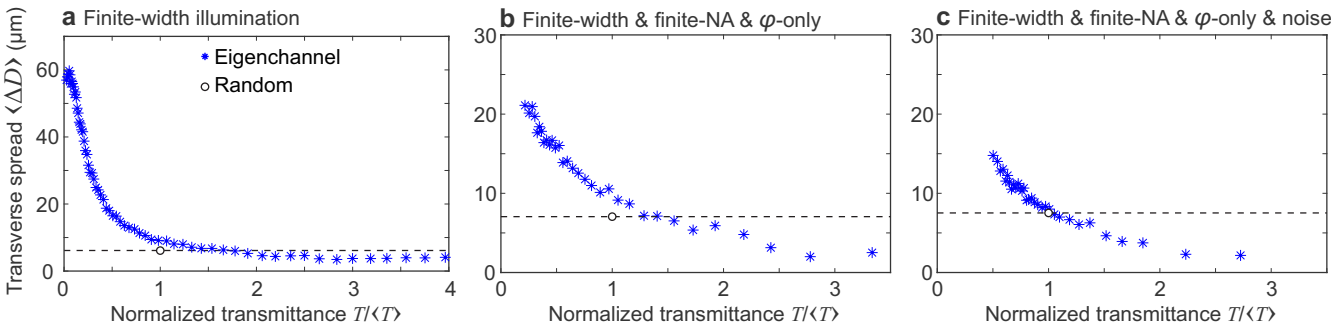

Figure S10. Transverse spread of transmission eigenchannels. Numerically calculated transverse spreading $\Delta D = D_{\text{out}} - D_{\text{in}}$ of transmission eigenchannels versus normalized transmittance $T/\langle T\rangle$. **a**, Only finite-width illumination is considered in the simulation, **b**, Including finite numerical aperture (NA) and phase-only (φ-only) modulation. **c**, Adding Gaussian random noise to the transmission matrix. In all cases, as $T/\langle T\rangle$ increases, ΔD decreases, indicating high-transmission channels spread less and low-transmission channels spread more than random incident wavefronts (black open circle and dashed line). The slab parameters are the same as those in Fig. 5 of the main text. Each data point represents an average over 50 disorder realizations.

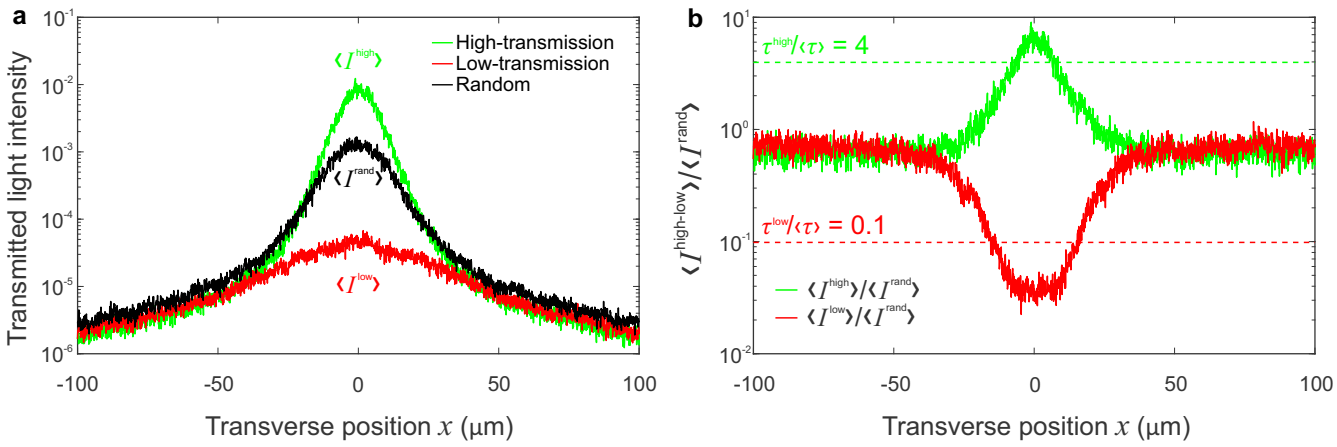

Figure S11. Transmitted light intensity profile of a diffusive slab with finite-width illumination. a, Spatial envelope of light intensity at the output surface of the slab for a high-transmission channel $\left(T^{\text{high}}/\langle T\rangle = 4\right)$, a low-transmission channel $\left(T^{\text{low}}/\langle T\rangle = 0.1\right)$, and a random incident wavefront, plotted by green, red, and black lines respectively. Each curve is an ensemble average over 50 disorder realizations. The slab parameters are the same as those in Fig. S10. **b**, Ratio of the transmitted light intensity envelope for high or low-transmission channel to that of random incident wavefront, $\langle I^{\text{high}}\rangle/\langle I^{\text{rand}}\rangle$ (green line), $\langle I^{\text{low}}\rangle/\langle I^{\text{rand}}\rangle$ (red line), illustrating the transmitted light intensity is enhanced or suppressed more at the centre than at the tails of the output beam.

given in the caption of Fig. 5 of the main text, are chosen to be close to those of the ZnO nanoparticle layer in our experiment. The slab ($n_0 = 1.4$) is sandwiched between air ($n_1 = 1.0$) and glass ($n_2 = 1.5$). Periodic boundary conditions are applied to the transverse boundaries. The number of input modes (from the air) is $N_1 = 1999 \approx 2n_1W/\lambda$, and the number of output modes (to the glass) $N_2 = 3239$. To model the binning of SLM pixels into macropixels and the limited field of view of detection optics, we group the input and output modes in k-space. The number of input modes in one group, m_1, is chosen such that the corresponding illumination width on the front surface of the slab, as given by the participation number of random inputs, is similar to that in the experiment. The number of output modes in a group, m_2, sets the size of detection region, which is similar to the field of view in our experiment (180 μm in diameter). Such grouping effectively reduces the number of degrees of freedom to $M_1 = 62$ at the input and $M_2 = 1079$ at the output.

The spatial profile of each transmission eigenchannel is then calculated. In Fig. S9 we plot the radial intensity profiles for high and low transmission eigenchannels in comparison to random incident wavefronts at front and back surfaces of the slab. At the front surface, only the high-transmission eigenchannel exhibits an exponential decay at the tail ($r = 4$ μm to 10 μm), while the random input profiles follow a sinc^2 function. On the back side, both high and low transmission channels feature exponential tails, so as the random input wavefronts. The decay length of the high-transmission channels is shorter than that of random incident wavefronts, while the low-transmission channels has a longer decay length than random inputs. Those results are in striking agreement with the experimental data in Fig. 5(h,i) of the main text.

The input and output widths are plotted in Fig. 5a of the main text, and the transverse spread is plotted as a function of the normalized transmittance in Fig. S10a. Low-transmission channels spread significantly more than random incident wavefronts, while high-transmission channels spread slightly less than random wavefronts with finite illumination width.

In order to account for finite NA in the experiment, we take only $M_1 = 32$ input degrees of freedom and $M_2 = 234$ output degrees of freedom in the k-space transmission matrix. The ratio $M_1/M_2 = 0.136$ is chosen to match that in the experiment, even though the experimental values of M_1 and M_2 are much larger. Additionally, we remove amplitude modulation from the input eigenvectors to simulate phase-only modulation in our experiment. As shown in Fig. S10b, the range for transverse spread of transmission eigenchannels is reduced, but the trend is similar to that in Fig. S10a.

Finally we use random Gaussian noise to model experimental errors in a transmission matrix measurement. We simulate the common-path interferometric measurement using the partial transmission matrix, adding random Gaussian numbers to the intensity values in the transmission to model detection noise. Such random Gaussian noise results in phase estimation errors in the "measured" transmission matrix, $\tilde{t} + \delta\tilde{t}$, which deviates from the actual matrix $\tilde{t}$ by $\delta\tilde{t}$. We calculate the transmission eigenvectors of this partial transmission matrix, remove their amplitude modulations, and then calculate their transmittance values and spatial profiles using the actual matrix $\tilde{t}$. The errors in the measurement of the transmission matrix cause a further reduction in the range of transmittance values and the lateral spread of the eigenchannels as Fig. S10c shows.

The above numerical simulation results illustrate that the

finite illumination width has a profound impact on the spatial profiles of transmission eigenchannels, making their behaviour qualitatively different from the eigenchannels of the complete transmission matrix for a wide slab. For comparison, we plot in Fig. S11a the intensity envelopes, obtained from ensemble average, on the output surface of the slab for a high-transmission eigenchannel $\langle I^{\text{high}} \rangle$ and a low-transmission eigenchannel $\langle I^{\text{low}} \rangle$, in comparison to a random wavefront $\langle I^{\text{rand}} \rangle$. Their ratios $\langle I^{\text{high}} \rangle / \langle I^{\text{rand}} \rangle$ and $\langle I^{\text{low}} \rangle / \langle I^{\text{rand}} \rangle$, plotted in Fig. S11b, reveal that the enhancement of transmitted light intensity is higher at the centre of the output beam for the high-transmission channel, leading to an effective reduction of the width (characterised by the participation number) of the output beam. For the low-transmission channel, the suppression of transmitted light intensity is also stronger at the beam centre, resulting in an increase of output beam-width. Such behaviour is attributed to the fact that multipath interference effects are enhanced near the centre of illumination region due to higher probability of scattering path crossing compared to the edges.

References

1. Popoff, S. M. *et al.* Measuring the transmission matrix in optics: an approach to the study and control of light propagation in disordered media. *Phys. Rev. Lett.* **104**, 100601 (2010).
2. Baranger, H. U., DiVincenzo, D. P., Jalabert, R. A. & Stone, A. D. Classical and quantum ballistic-transport anomalies in microjunctions. *Phys. Rev. B* **44**, 637–675 (1991).
3. Durian, D. J. Influence of boundary reflection and refraction on diffusive photon transport. *Phys. Rev. E* **50**, 857–866 (1994).
4. Yamilov, A. Relation between channel and spatial mesoscopic correlations in volume-disordered waveguides. *Phys. Rev. B* **78**, 045104 (2008).
5. Shi, Z. & Genack, A. Z. Diffusion in translucent media. *Nat. Commun.* **9**, 1862 (2018).
6. Ishimaru, A. *Wave Propagation and Scattering in Random Media* (Academic, New York, 1978).
7. Izrailev, F. M. Simple models of quantum chaos: spectrum and eigenfunctions. *Phys. Rep.* **196**, 299–392 (1990).
8. Casati, G., Molinari, L. & Izrailev, F. Scaling properties of band random matrices. *Phys. Rev. Lett.* **64**, 1851–1854 (1990).
9. Fyodorov, Y. V. & Mirlin, A. D. Analytical derivation of the scaling law for the inverse participation ratio in quasi-one-dimensional disordered systems. *Phys. Rev. Lett.* **69**, 1093–1096 (1992).